Geophysical Research Letters

RESEARCH LETTER
10.1029/2022GL100463

**Key Points:**

- Poleward shifts of the Southern Hemisphere extratropical jet stream change atmospheric cloud radiative heating through two key mechanisms
- The fraction of low clouds that are exposed to space increases equatorward of the mean jet latitude, enhancing local radiative cooling
- Clouds in extratropical cyclones shift poleward, causing radiative heating anomalies throughout the troposphere

**Supporting Information:**

Supporting Information may be found in the online version of this article.

**Correspondence to:**

C. J. Wall,
casey.wall@geo.uio.no

**Citation:**

Wall, C. J., Lutsko, N. J., & Vishny, D. N. (2022). Revisiting cloud radiative heating and the Southern Annular Mode. *Geophysical Research Letters*, *49*, e2022GL100463. https://doi.org/10.1029/2022GL100463

Received 15 JUL 2022
Accepted 26 SEP 2022

**Author Contributions:**

**Conceptualization:** Casey J. Wall
**Formal analysis:** Casey J. Wall
**Funding acquisition:** Nicholas J. Lutsko
**Investigation:** Casey J. Wall
**Methodology:** Casey J. Wall
**Project Administration:** Nicholas J. Lutsko
**Resources:** Nicholas J. Lutsko
**Software:** Casey J. Wall
**Validation:** David N. Vishny
**Visualization:** Casey J. Wall
**Writing – original draft:** Casey J. Wall
**Writing – review & editing:** Nicholas J. Lutsko, David N. Vishny



# Revisiting Cloud Radiative Heating and the Southern Annular Mode

**Casey J. Wall[1,2], Nicholas J. Lutsko[1], and David N. Vishny[1]**

[1]Scripps Institution of Oceanography, University of California San Diego, La Jolla, CA, USA, [2]Now at Department of Geosciences, University of Oslo, Oslo, Norway

**Abstract** Cloud-circulation interactions have a potentially large but uncertain influence on regional climate. Here we use satellite observations to investigate relationships between atmospheric cloud radiative heating and hemispheric-scale shifts in the Southern Hemisphere extratropical jet stream, as represented by the Southern Annular Mode. In contrast to a previous study, we find that poleward jet shifts cause bottom-heavy heating anomalies. The heating anomalies arise from two distinct mechanisms: First, poleward jet shifts promote anomalous large-scale subsidence equatorward of the mean jet latitude. This increases the fraction of low clouds that are exposed to space, thereby enhancing lower-tropospheric radiative cooling. Second, deep and multi-layer clouds in extratropical cyclones shift poleward with the jet, causing radiative heating anomalies throughout the troposphere. The bottom-heavy structure of the heating anomalies occurs because low clouds strongly emit radiation. These results establish new observational benchmarks for understanding extratropical cloud-circulation interactions.

**Plain Language Summary** Atmospheric circulation controls cloud formation, and clouds change atmospheric radiative and latent heating, thereby affecting the circulations in which they form. These two-way interactions affect regional climate by a potentially large but uncertain amount. Here we use satellite data to investigate relationships between cloud radiative heating and poleward shifts of the extratropical jet stream in the Southern Hemisphere. We show that poleward jet shifts cause bottom-heavy radiative heating anomalies throughout the extratropics. These heating anomalies result from an increase in the low-cloud fraction equatorward of the mean jet-stream latitude and a poleward shift of clouds in extratropical cyclones. The bottom-heavy heating structure occurs because low-level clouds strongly emit radiation. These observed relationships advance our understanding of cloud-circulation interactions in the extratropics.

## 1. Introduction

Clouds and atmospheric circulation are intimately linked through two-way interactions. Rising air currents form clouds, and clouds perturb diabatic heating of the atmosphere, thereby changing the circulations in which they are embedded. This two-way interaction shapes patterns of regional climate variability and change (Bony et al., 2015; Voigt & Shaw, 2015, 2016).

One way that clouds affect circulation is by changing radiative heating of the atmosphere. In the tropics, cloud radiative heating is known to affect large-scale overturning circulations and the clustering of deep convection (Emanuel et al., 2013; Hartmann et al., 1984). In the extratropics, however, interactions among clouds, radiation, and circulation are not as well understood. Modeling studies have shown that cloud radiative heating dampens the intensity of extratropical cyclones and shifts the mean position of the extratropical jet (Grise et al., 2019; Schäfer & Voigt, 2018; Watt-Meyer & Frierson, 2017), but the effects on hemispheric-scale variability are contested and poorly understood on a theoretical level (Li, Thompson, Huang, & Zhang, 2014; Papavasileiou et al., 2020; Voigt et al., 2021).

Here we use satellite observations to investigate links between cloud radiative heating and hemispheric-scale extratropical variability. In particular, we examine how cloud radiative heating responds to meridional shifts of the extratropical jet stream in the Southern Hemisphere, as represented by the Southern Annular Mode (SAM). Li and Thompson (2016) diagnosed coherent patterns of cloud radiative heating that arise from SAM variations. We extend their analysis by decomposing the radiative heating response into contributions from particular cloud regimes, and we explain the relative importance of the different regimes by analyzing radiative heat budgets

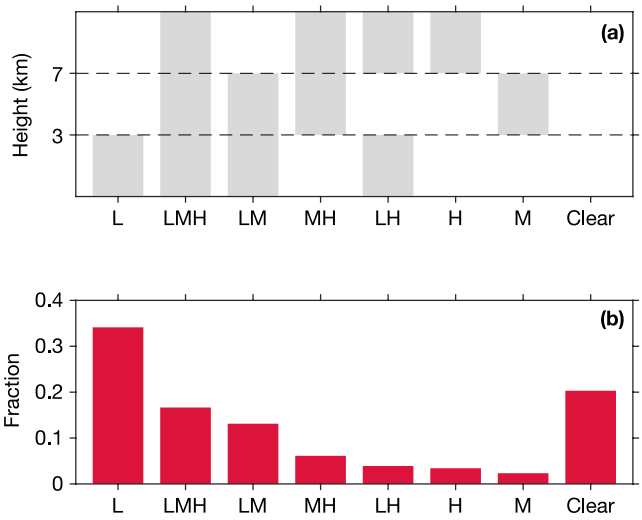


**Figure 1.** Description and statistics of the cloud regimes. (a) Schematic of the regime definitions. Gray indicates that a cloud exists somewhere within the vertical interval, and white indicates that no clouds exist within the vertical interval. (b) Mean area fraction of the regimes between 30° and 75°S.

of idealized clouds. We conclude by discussing how the results can be leveraged by modeling studies to investigate extratropical cloud-circulation interactions.

## 2. Data and Methods

We study instantaneous vertical profiles of cloud properties and radiative fluxes retrieved from radar and lidar measurements of the CloudSat and CALIPSO satellites (Stephens et al., 2002). Profiles of longwave (LW) radiative fluxes, volumetric cloud fraction $c$, temperature, and pressure are obtained from the CloudSat data products 2B-FLXHR-LIDAR version P1_R05, 2B-GEOPROF-LIDAR version P2_R05, and ECMWF-AUX version P_R05 (Henderson et al., 2013; L'Ecuyer et al., 2008; Mace & Zhang, 2014). For a given height interval, $c$ is defined as the percentage of volumes in which the radar or lidar detect hydrometeors. We also compute the atmospheric LW cloud radiative heating rate $R$, which quantifies how much clouds change atmospheric radiative heating relative to clear sky:

$$R = \frac{g}{c_p}\left(\frac{dF_{\mathrm{LW,act}}}{dp} - \frac{dF_{\mathrm{LW,clr}}}{dp}\right).$$

Here $g$ is the gravitational constant, $c_p$ is the specific heat capacity of dry air at constant pressure, $p$ is pressure, $F_{\mathrm{LW,act}}$ is the actual net upward flux of LW radiation, and $F_{\mathrm{LW,clr}}$ is the net upward flux of LW radiation that would occur if clouds were removed, leaving all else unchanged. We neglect cloud heating from shortwave radiation because it is much smaller than LW heating at regional scales (Haynes et al., 2013; Voigt et al., 2021). All variables are zonally averaged over 2.5° latitude bins, 5-day time bins, and 480 m height bins. Statistical analysis is performed with the zonal-mean pentad-mean data between 30°S and 75°S and from 2007 through 2010.

We also classify each instantaneous profile into one of eight regimes based on cloud vertical structure. Profiles that include a cloud anywhere below 3 km receive an "L" label, profiles that include a cloud anywhere between 3 and 7 km receive an "M" label, and profiles that include a cloud anywhere above 7 km receive an "H" label. This classification method is similar to that of Oreopoulos et al. (2017). Because clouds can simultaneously exist at different heights, seven cloud regimes are possible: L, M, H, LM, MH, LH, and LMH (Figure 1a). The final regime is clear sky. For a given regime $i$, the area fraction of the regime, $f_i$, is defined as the fraction of profiles that are assigned to the regime. We compute $f_i$ for each pentad and 2.5° latitude bin. Most profiles are assigned to one of the regimes containing the L label because low-level clouds are common over the Southern Ocean (Figure 1b).

Variability of the large-scale barotropic circulation is characterized by the SAM (Thompson & Wallace, 2000). The SAM index $s$ is defined as the leading principal component timeseries of daily-mean zonal-mean zonal wind over all latitudes and pressure levels between 20° and 70°S and 1,000 and 200 hPa (Thompson & Woodworth, 2014). The wind field used to calculate $s$ is computed by taking daily averages of six-hourly winds between 1979 and 2018 from ERA5 reanalysis (Hersbach et al., 2020), then removing the climatological seasonal cycle. We average $s$ over 5-day intervals and standardize the time series. Positive $s$ values indicate that the strongest westerly winds are shifted poleward relative to the climatology, and vice versa for negative $s$ values (Figure S1a in Supporting Information S1; Gelaro et al., 2017). To quantify this relationship, we relate the latitude of the extratropical jet to $s$ using ordinary least squares regression. The jet latitude $\phi_j$ is defined as the maximum zonal-mean zonal wind at 850 hPa, and it is computed by fitting a quadratic polynomial to the grid point of maximum wind and the two neighboring points on either side (Watt-Meyer & Frierson, 2017). According to this definition, $d\phi_j/ds = -2.7 \pm 0.4°\sigma_s^{-1}$, where $\sigma_s$ is the standard deviation of $s$ (95% confidence).

We also use linear regression to relate cloud variations to $s$. For each joint latitude-height bin, we remove the time averages of $c$ and $R$ computed over the entire record. The seasonal cycle is not removed because the data record is relatively short, but $s$ is uncorrelated with the day of the year by definition, so seasonal variations of $c$ and $R$ are uncorrelated with $s$. The anomalies of $c$ and $R$ are regressed against $s$ to estimate $dc/ds$ and $dR/ds$. We also

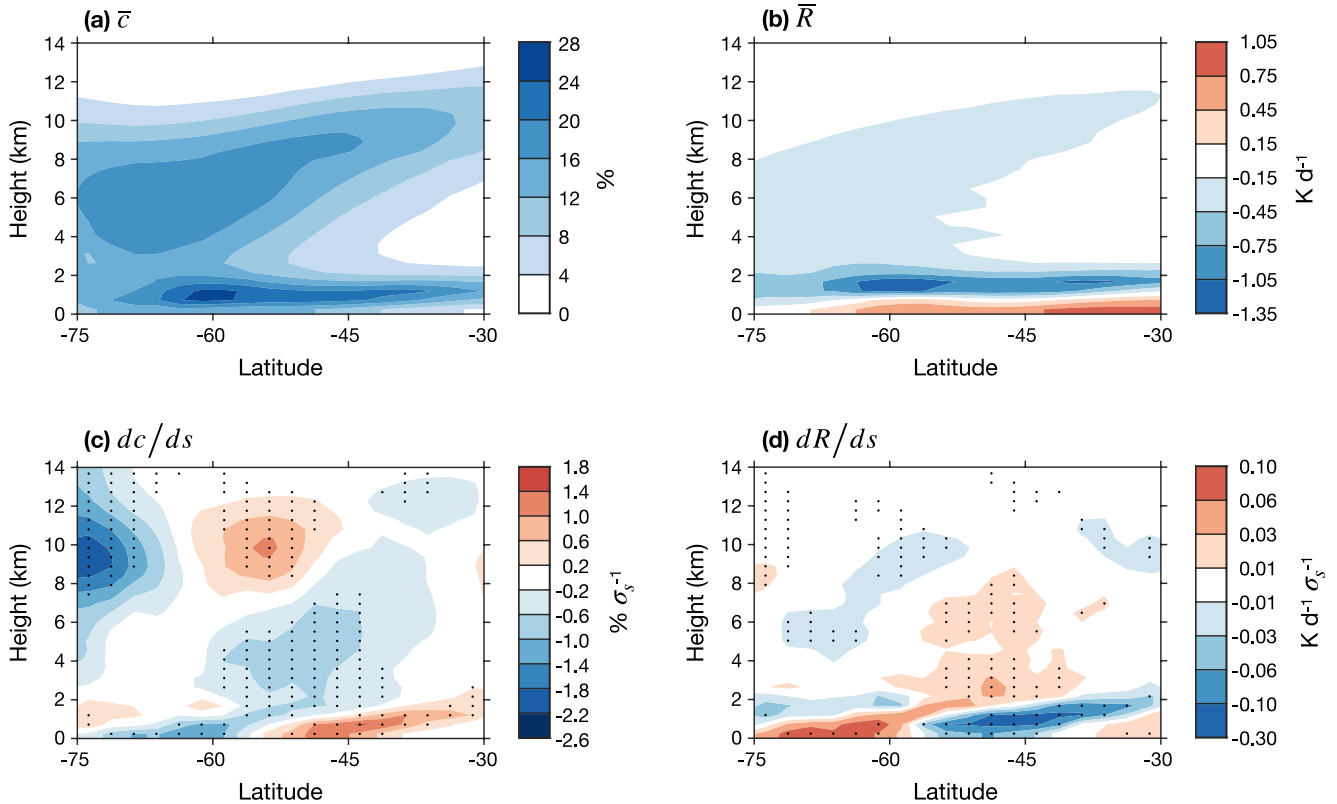


**Figure 2.** Cloud climatology and response to Southern Annular Mode (SAM) variability. (a and b) Mean volumetric cloud fraction $c$ and atmospheric LW cloud radiative heating rate $R$. Overbars denote zonal-mean time-mean values. (c and d) Linear regression coefficients representing changes in $c$ and $R$ in response to a one-standard-deviation increase in the SAM index $s$. Stippling denotes coefficients that are significantly different from zero at the 95% confidence level. Note that the contours are not uniformly spaced in panel (d).

decompose $dR/ds$ into contributions from the different cloud regimes. For a given latitude-height bin, let $R_i$ represent the average of $R$ computed over the profiles assigned to cloud regime $i$. $R$ can then be expressed as the sum of $f_i R_i$ over the seven cloud regimes. Thus, $dR/ds$ can be decomposed according to

$$\frac{dR}{ds} = \sum_{i=1}^{7} \left( \frac{df_i}{ds}\overline{R}_i + \overline{f}_i \frac{dR_i}{ds} \right), \tag{1}$$

where overbars indicate the time average of a quantity. The term $\frac{df_i}{ds}\overline{R}_i$ represents heating anomalies that are caused by changes in the area fraction of regime $i$, and the term $\overline{f}_i \frac{dR_i}{ds}$ represents heating anomalies that are caused by changes in the average heating profile of regime $i$. The second component includes the effects of changes in temperature, humidity, and regime-average cloud properties such as cloud-top height, cloud-base height, and cloud optical thickness. We compute $\overline{R}_i$ and $\overline{f}_i$ by averaging over the entire time record, and we regress anomalies of $f_i$ and $R_i$ against $s$ to estimate $df_i/ds$ and $dR_i/ds$. These estimates accurately reproduce $dR/ds$ through the decomposition in Equation 1 (Figure S2 in Supporting Information S1). We therefore use the decomposition to determine how much each cloud regime contributes to $dR/ds$. Regression-coefficient uncertainty is quantified following the method of Bretherton et al. (1999) as described in the Supporting Information S1.

## 3. Response of Cloud Radiative Heating to the SAM

We first examine the cloud climatology over the Southern Hemisphere extratropics to establish the background conditions on which SAM-induced cloud variations are superposed. The $\overline{c}$ profile has a bimodal distribution, including one local maximum around 1 km that is associated with low-level clouds and a second local maximum between 6 and 10 km that is associated with free-tropospheric clouds (Figure 2a; Wall et al., 2017). The cloud population affects the mean radiative heating rate of the atmosphere by absorbing and emitting LW radiation.

Cloud absorption and emission depend on cloud temperature, cloud emissivity, and the conditions of the underlying and overlying environment, but absorption typically dominates near cloud base and emission typically dominates near cloud top. Thus, low clouds cause a heating-cooling dipole pattern that is centered around 1 km in the profile of $\overline{R}$ (Figure 2b). Higher clouds enhance the radiative cooling rate of the free troposphere, but this cooling effect is smaller in magnitude than the heating-cooling dipole caused by low-level clouds. We find similar results when we calculate $\overline{R}$ using the CALIPSO-CloudSat-CERES-MODIS data set (Kato et al., 2021), which uses different retrieval algorithms, and we find similar results when we calculate $\overline{R}$ by inputting profiles of cloud optical thickness, temperature, and humidity into the Rapid Radiative Transfer Model for Global Climate Models (Figures S3 and S4 in Supporting Information S1; Clough et al., 2005; Slingo, 1989; Fu, 1996). Furthermore, our estimates of $\overline{R}$ are qualitatively consistent with those of Haynes et al. (2013) and Ham et al. (2017). The consistency among these results shows that our estimates of $R$ are robust.

The dynamical variations associated with the SAM cause clouds to vary relative to the climatology shown in Figures 2a and 2b. We first examine the variations of $c$ using linear regression. The regression coefficients for $dc/ds$ represent the cloud-fraction response to a one-standard-deviation increase in $s$, which indicates a poleward shift of the extratropical jet. The pattern of $dc/ds$ has a three-tiered vertical structure, including a horizontal dipole pattern between 7 and 13 km and 75° and 50°S, reduced cloud fraction between 1.5 and 7 km and 60° and 40°S, and a horizontal dipole pattern below 1.5 km and between 75° and 30°S (Figure 2c). Li and Thompson (2016) showed that these cloud anomalies coincide with several anomalies of the meteorological environment. First, $c$ anomalies above 7 km coincide with anomalies of the static stability and temperature of the upper troposphere, suggesting that they are associated with vertical shifts of the tropopause. Second, $c$ reductions between 1.5 and 7 km coincide with anomalous large-scale downward motion that is caused by poleward expansion of the Hadley circulation and a poleward shift of the extratropical jet. Third, $c$ anomalies below 1.5 km coincide with anomalous low-level static stability, suggesting that they may result from anomalies of the inversion strength at the top of the planetary boundary layer. Lipat et al. (2018) also showed modeling evidence that poleward expansion of the Hadley circulation causes stronger middle-tropospheric subsidence and enhanced lower-tropospheric stability between about 35° and 55°S. We find that SAM variations are related to anomalies of tropopause pressure, middle-tropospheric vertical motion, and lower-tropospheric stability in ways that are consistent with these studies (Figure S1 in Supporting Information S1). Collectively these meteorological anomalies likely explain much of the pattern of $dc/ds$.

The SAM-induced cloud-fraction anomalies affect $R$ across the Southern Hemisphere extratropics. The large-scale pattern of $dR/ds$ includes one meridional dipole between 2 and 10 km and a second dipole of opposite sign below 2 km (Figure 2d). Peak values of $dR/ds$ below 2 km are an order of magnitude larger than those above 2 km, meaning that the vertical profile of $dR/ds$ is bottom heavy. We obtain similar $dR/ds$ estimates using radiative fluxes from the CALIPSO-CloudSat-CERES-MODIS data set (Kato et al., 2021; Figure S3 in Supporting Information S1). Thus, our results robustly show that SAM variations change vertical and horizontal gradients of $R$, especially in the lower troposphere.

The estimate of $dR/ds$ can be further understood by examining the contributions of different cloud regimes. We begin by examining the contribution of the L regime, which is the most common regime between 30° and 75°S (Figure 1b). L clouds emit more radiation than they absorb near cloud top, and they emit less radiation than they absorb near cloud base, so the regime-average heating profile, $\overline{R}_L$, is negative between 1 and 3 km and positive near the surface (Figure 3a). Furthermore, as $s$ increases, the fraction of L clouds increases between 50° and 30°S (Figure 3b). This cloud response is likely caused by anomalous downward motion in the free troposphere that is associated with poleward expansion of the Hadley circulation and a poleward shift of the extratropical jet. We estimate the total contribution of L clouds to $dR/ds$ by summing the component associated with changes in the area fraction of L clouds, $\overline{R}_L df_L/ds$, and the component associated with changes in the average heating profile of L clouds, $\overline{f}_L dR_L/ds$ (Equation 1). The second term includes the effect of changes in the average cloud-top height of L clouds, which can shift the height of peak radiative cooling. This estimate reveals that changes in L clouds are responsible for most of the relatively large $R$ anomalies that occur below 3 km across the Southern Hemisphere extratropics (Figure 3c). L clouds therefore make a major contribution to $dR/ds$.

The second most common cloud regime over the Southern Ocean is LMH (Figure 1b). These deep or multi-layer clouds cause anomalous radiative cooling above 6 km and anomalous radiative heating below (Figure 3d).

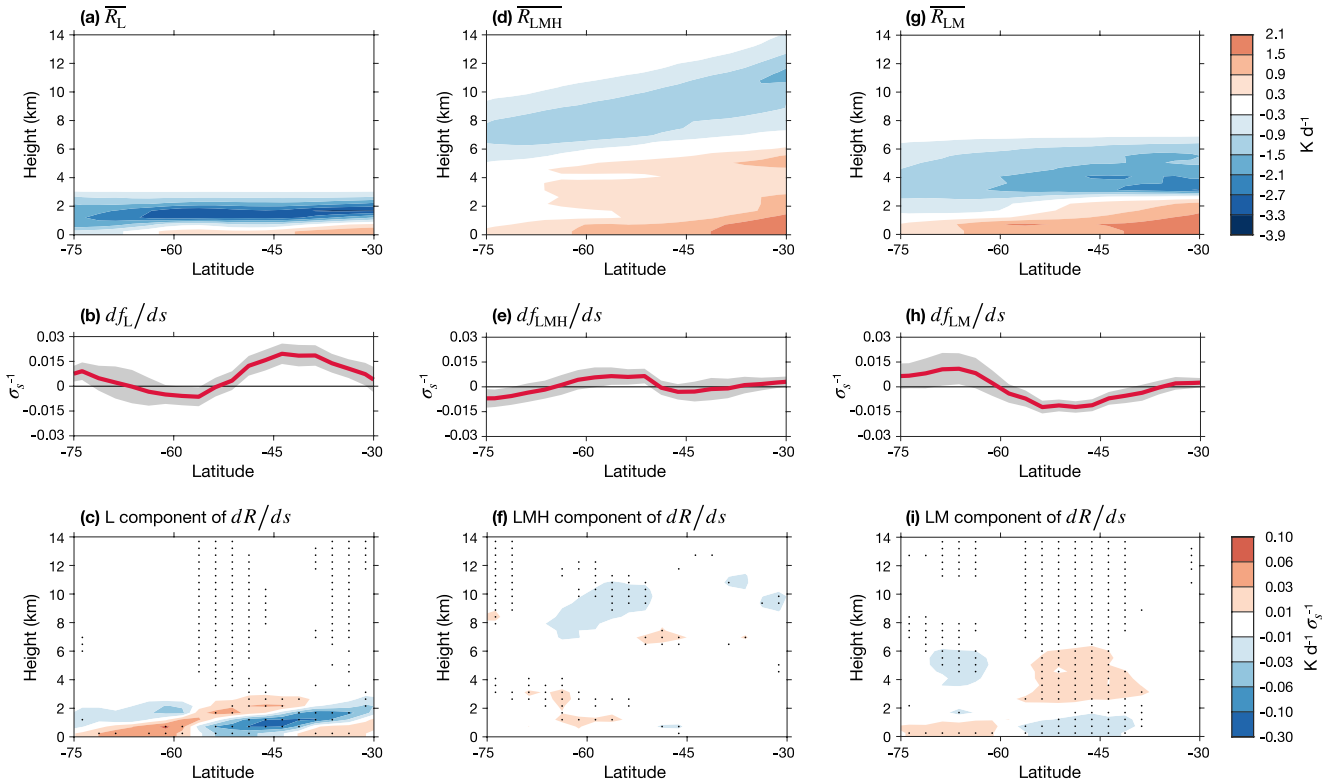


**Figure 3.** Contributions of the three most common cloud regimes to $dR/ds$. (a) Average cloud radiative heating profile for the L regime, $\overline{R_L}$. (b) Linear regression coefficients representing the change in $f_L$ in response to a one-standard-deviation increase in $s$. (c) The contribution of L clouds to $dR/ds$ . Gray shading in (b) shows the 95% confidence interval, and stippling in (c) indicates values that are significantly different from zero at the 95% confidence level. Panels (d–f) and (g–i) are similar to (a–c), except that they show the LMH and LM cloud regimes, respectively. Note that the contours are not uniformly spaced in (c, f, and i).

Although upper-tropospheric clouds often cause local warming, the cloud below 7 km in the LMH regime reduces the upward LW flux that reaches the upper troposphere. This weakens LW absorption in the upper troposphere and causes $\overline{R_{LMH}}$ to be negative there (Hartmann et al., 2001). Furthermore, $df_{LMH}/ds$ is either insignificant or smaller in magnitude than $df_L/ds$ at all latitudes (Figure 3e). This relatively weak relationship could be a consequence of several mechanisms. LMH clouds within extratropical cyclones are expected to shift poleward as $s$ increases, but positive $s$ anomalies are also associated with weaker static stability between about 7 and 12 km and 40° and 55°S, and vice versa between 60° and 75°S (Li & Thompson, 2016). The change in upper-tropospheric stability acts to decrease upper-tropospheric cloudiness poleward of 60°S and increase upper-tropospheric cloudiness equatorward of 55°S (Li, Thompson, Stephens, & Bony, 2014). This counteracts the changes in upper-tropospheric cloudiness that are caused by poleward shifts of cyclones. Because of the relatively weak relationship between $f_{LMH}$ and $s$, LMH clouds contribute modestly to $dR/ds$ (Figure 3f).

The third most common cloud regime is LM. This regime often exists within extratropical cyclones, and it can include large cumulus clouds that occur in unstable environments in the cold-advection sector and multi-layer clouds that occur in the warm-advection sector (Field & Wood, 2007; Govekar et al., 2011). LM clouds cause negative $R$ anomalies between about 2 and 7 km and positive $R$ anomalies below 2 km (Figure 3g). Furthermore, because extratropical cyclones shift poleward in response to increasing $s$, LM clouds shift poleward as well. This causes a meridional dipole pattern of $df_{LM}/ds$ (Figure 3h). The combination of poleward shifts of LM clouds and changes in their regime-average $R$ profile contributes significantly to $dR/ds$ across most of the Southern Hemisphere extratropics (Figure 3i). The LM component of $dR/ds$ is smaller in magnitude than the L component, but it explains most of $dR/ds$ between about 3 and 7 km. LM clouds therefore make a distinct and significant contribution to $dR/ds$.

The remaining four cloud regimes contribute much less to $dR/ds$ (Figure S5 in Supporting Information S1). Some regimes make a small contribution because the regime-average heating rate is relatively small (i.e., $|\overline{R_i}|$

and $|dR_i/ds|$ are small), and others make a small contribution because they cover a small area (i.e., $|\overline{f_i}|$ and $|df_i/ds|$ are small). The cloud-regime analysis therefore reveals two key mechanisms by which clouds responds to increasing $s$: First, anomalous large-scale downward motion on the equatorward side of average jet-stream latitude increases the fraction of L clouds, thereby enhancing radiative cooling of the lower troposphere. Second, the poleward shift of extratropical cyclones shifts LM clouds poleward, causing $R$ anomalies throughout the troposphere. These two mechanisms explain most of the large-scale pattern of $dR/ds$.

## 4. Radiative Heat Budgets of Idealized Single-Layer Clouds

We next frame our results in the context of the existing literature to examine the implications for cloud-circulation interactions. Li and Thompson (2016) first diagnosed relationships between clouds and SAM variability using satellite observations. They analyzed a binary estimate of $c$ called "cloud incidence," but we verified that the regressions of cloud incidence against $s$ are approximately equal to the regressions of $c$ against $s$. Compared with our results, Li and Thompson (2016) estimate similar values for $dc/ds$, but their $dR/ds$ estimate is an order of magnitude larger above 4 km and an order of magnitude smaller below 4 km (their Figures 1c and 5a). In other words, the two estimates disagree on whether $dR/ds$ is top heavy or bottom heavy. This difference may have implications for the interactions between cloud radiative heating and SAM variability because top- and bottom-heavy $R$ anomalies affect static stability and horizontal temperature gradients in different ways.

We investigate the discrepancy between the $dR/ds$ estimates by computing cloud radiative heating profiles using the Rapid Radiative Transfer Model for Global Climate Models (RRTMG; Clough et al., 2005). Our RRTMG calculations approximately reproduce observational estimates of $R$ (Figure S4 in Supporting Information S1), so in this section we use the model to examine radiative heating of idealized single-layer clouds. The idealized clouds are assumed to contain ice particles with an effective radius of 30 $\mu$m where the temperature is colder than 253 K, and they are assumed to contain liquid droplets with an effective radius of 10 $\mu$m otherwise. We assume that the clouds are overcast, they occupy a layer of thickness $\delta p = 50$ hPa, and they have a typical condensed water path of 80 g m$^{-2}$ based on observations reported by McCoy et al. (2014). Clouds with these properties are optically thick in the LW band, so the results are similar if the condensed water path is changed by $\pm$ 50% (not shown). We also use the average atmospheric temperature and humidity profile between 40° and 70°S, and we assume concentrations of well-mixed greenhouse gases that are consistent with the CloudSat retrieval algorithms (Supporting Information S1). Finally, we vary the cloud-top height (CTH) to examine how clouds at different elevations contribute to the vertical structure of $R$.

We begin by examining the bulk radiative heat budget of the idealized clouds. Let $[R]$ represent the mass-weighted vertical average of $R$ across the cloud layer. This term can be expressed as:

$$[R] = A + E - [R_{\mathrm{clr}}]$$

where $A$ is the heating rate caused by total LW absorption, $E$ is the heating rate caused by total LW emission, and $[R_{\mathrm{clr}}]$ is the clear-sky heating rate averaged over the level occupied by the cloud. Because the cloud is optically thick in the LW band,

$$A = \frac{g}{c_p \delta p}\left(\mathrm{LW}_{\downarrow,\mathrm{t}} + \mathrm{LW}_{\uparrow,\mathrm{b}}\right)$$

and

$$E = -\frac{g}{c_p \delta p}\left(\mathrm{LW}_{\downarrow,\mathrm{b}} + \mathrm{LW}_{\uparrow,\mathrm{t}}\right),$$

where $\mathrm{LW}_{\downarrow}$ and $\mathrm{LW}_{\uparrow}$ are downward and upward LW fluxes, and the subscripts "t" and "b" indicate cloud top and cloud base, respectively. As the cloud rises, it becomes colder, the incident LW radiation at cloud base increasingly originates from the underlying atmosphere rather than the surface, and the incident LW radiation at cloud top increasingly originates from a colder and optically thinner overlying atmosphere. These effects weaken $A$ and $E$ (Figure 4a). Furthermore, $[R_{\mathrm{clr}}]$ is approximately constant with height, so changes in the relative amounts of absorption and emission determine how $[R]$ varies with CTH (Jeevanjee & Fueglistaler, 2020). Emission dominates when CTH is below 9 km, and absorption dominates otherwise. Emission also changes more rapidly with

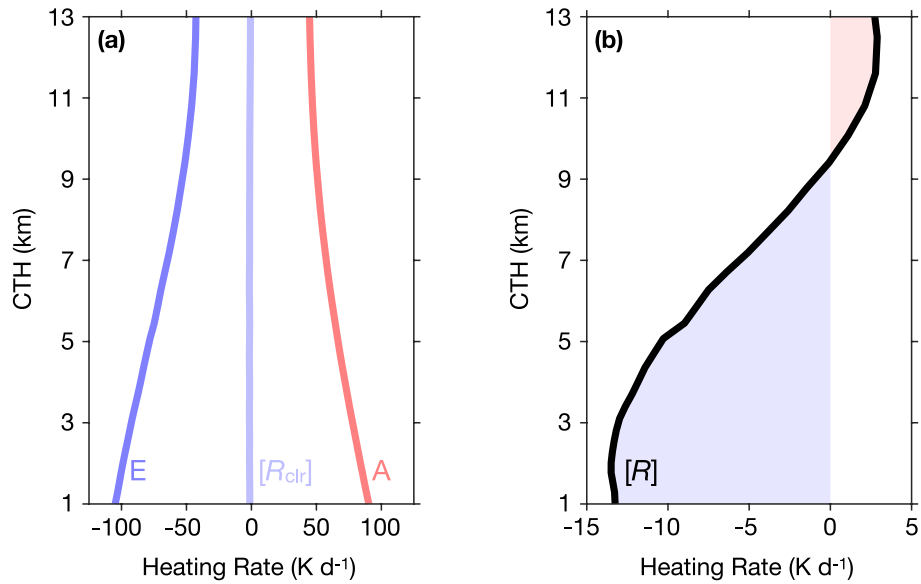


**Figure 4.** Radiative heat budget of an idealized overcast single-layer cloud plotted as a function of cloud-top height (CTH). (a) Heating-rate terms from the radiative heat budget, including total longwave (LW) emission ($E$), total LW absorption ($A$), and clear-sky radiative heating averaged over the layer occupied by the cloud ($[R_{clr}]$). (b) Cloud radiative heating rate averaged over the cloud layer ($[R]$). Blue shading indicates negative $[R]$, and vice versa for red shading.

height than absorption, so the local cooling effect of a cloud with CTH between 1 and 3 km is about six times larger than the local warming effect of a cloud with CTH between 10 and 13 km (Figure 4b). This helps to explain why the climatology of $R$ is bottom heavy (Figure 2).

We are now in a position to examine the vertical structure of $dR/ds$ using scale analysis and our idealized clouds. Our observational estimate of $dR/ds$ is bottom heavy and has peak zonal-mean heating anomalies of about $\pm$ 0.17 K d$^{-1}$ $\sigma_s^{-1}$ around 1 km (Figure 2). Furthermore, our idealized cloud with a top at 1.1 km has an overcast heating rate of $[R] = -13$ K d$^{-1}$ (Figure 4). Thus, if $f^*$ represents the area fraction covered by the idealized cloud, then $|df^*/ds| = 0.012\,\sigma_s^{-1}$ would produce values of $dR/ds$ that are commensurate with our observational estimate. This value of $df^*/ds$ is consistent with observed changes in low-cloud fraction in response to SAM variations (Figure 3). In contrast, Li and Thompson (2016) report a top-heavy profile of $dR/ds$ with peak zonal-mean heating anomalies of about $\pm$ 0.28 K d$^{-1}$ $\sigma_s^{-1}$ between 7 and 9 km (their Figure 5a). Our idealized cloud with a top at 8.2 km has an overcast heating rate of $[R] = -2.6$ K d$^{-1}$ (Figure 4). In this case, $|df^*/ds|$ would need to be 0.11 $\sigma_s^{-1}$ to produce values of $dR/ds$ that are commensurate with Li and Thompson's (2016) estimate. This change in cloud fraction is an order of magnitude larger than observed changes in the fraction of all regimes containing clouds above 7 km (Figure 3, Figure S5 in Supporting Information S1). Thus, a bottom-heavy pattern of $dR/ds$ is realistic, but a top-heavy pattern is not.

## 5. Summary and Discussion

Interactions between clouds and large-scale atmospheric circulation affect regional climate variability and change by a potentially large but uncertain amount. Here we investigate cloud-circulation interactions that are associated with natural variability of the SAM. We show that a poleward shift of the extratropical jet stream changes cloud radiative heating through two key mechanisms. First, poleward jet shifts promote anomalous large-scale subsidence in the free troposphere equatorward of the mean jet latitude. This increases the fraction of L clouds, thereby enhancing radiative cooling of the lower troposphere. Second, LM clouds shift poleward with the jet, causing $R$ anomalies throughout the troposphere (Figure 3). Collectively these mechanisms produce a bottom-heavy profile of $dR/ds$, in contrast to a previous observational estimate (Li & Thompson, 2016). The bottom-heavy structure of the heating anomalies occurs because low clouds strongly emit LW radiation (Figure 4).

Our findings provide new observational benchmarks for understanding how variations of the large-scale extratropical circulation affect cloud radiative heating. An important next step is to understand how the heating anomalies, in turn, affect the circulation. This could be accomplished by running idealized general circulation models with prescribed radiative heating patterns that mimic the overall $dR/ds$ and the heating contributions of the different cloud regimes. The observed relationships could also be used to evaluate cloud parameterizations in comprehensive climate models, in which large-scale circulation is resolved but individual clouds are not. These next steps would lead to a richer understanding of cloud-circulation interactions in the extratropics.

## Data Availability Statement

All data used in this study are publicly available. CloudSat data products 2B-FLXHR-LIDAR, 2B-GEOPROF-LIDAR, and ECMWF-AUX are available from the CloudSat DPC website (https://www.cloudsat.cira.colostate.edu/data-products). The CALIPSO-CloudSat-CERES-MODIS data set is available from the CERES ordering tool (https://ceres-tool.larc.nasa.gov/ord-tool/products?CERESProducts=CCCM). ERA5 data are available from the Copernicus Climate Change Service Climate Data Store (https://cds.climate.copernicus.eu/#!/search?text=ERA5&type=dataset). MERRA-2 data are available from the NASA Earthdata website (https://search.earthdata.nasa.gov/). Matlab code for the analysis in this study is available at https://github.com/nicklutsko/CRE_Southern_Annular_Mode.

**Acknowledgments**
The authors thank Shim Yook for sharing the *s* timeseries. C.J.W., N.J.L., and D.N.V. were supported by the NOAA Climate Program Office's Modeling, Analysis, Predictions, and Projections program through grant NA20OAR4310387.

## References

Bony, S., Stevens, B., Frierson, D. M. W., Jakob, C., Kageyama, M., Pincus, R., et al. (2015). Clouds, circulation and climate sensitivity. *Nature Geoscience*, *8*(4), 261–268. https://doi.org/10.1038/ngeo2398

Bretherton, C. S., Widmann, M., Dymnikov, V. P., Wallace, J. M., & Blade, I. (1999). Effective number of degrees of freedom of a spatial field. *Journal of Climate*, *12*(1969), 1990–2009. https://doi.org/10.1175/1520-0442(1999)012<1990:Tenosd>2.0.Co;2

Clough, S. A., Shephard, M. W., Mlawer, E. J., Delamere, J. S., Iacono, M. J., Cady-Pereira, K., et al. (2005). Atmospheric radiative transfer modeling: A summary of the AER codes. *Journal of Quantitative Spectroscopy and Radiative Transfer*, *91*(2), 233–244. https://doi.org/10.1016/j.jqsrt.2004.05.058

Emanuel, K., Wing, A. A., & Vincent, E. M. (2013). Radiative-convective instability. *Journal of Advances in Modeling Earth Systems*, *6*(1), 75–90. https://doi.org/10.1002/2013MS000270

Field, P. R., & Wood, R. (2007). Precipitation and cloud structure in midlatitude cyclones. *Journal of Climate*, *20*(2), 233–254. https://doi.org/10.1175/JCLI3998.1

Fu, Q. (1996). An accurate parameterization of the solar radiative properties of cirrus clouds for climate models. *Journal of Climate*, *9*, 2058–2081. https://doi.org/10.1175/1520-0442(1996)009<2058:aapots>2.0.co;2

Gelaro, R., McCarty, W., Suárez, M. J., Todling, R., Molod, A., Takacs, L., et al. (2017). The modern-era retrospective analysis for research and applications, version 2 (MERRA-2). *Journal of Climate*, *30*(14), 5419–5454. https://doi.org/10.1175/jcli-d-16-0758.1

Govekar, P. D., Jakob, C., Reeder, M. J., & Haynes, J. (2011). The three-dimensional distribution of clouds around southern hemisphere extratropical cyclones. *Geophysical Research Letters*, *38*(21), 1–6. https://doi.org/10.1029/2011GL049091

Grise, K. M., Medeiros, B., Benedict, J. J., & Olson, J. G. (2019). Investigating the influence of cloud radiative effects on the extratropical storm tracks. *Geophysical Research Letters*, *46*(13), 7700–7707. https://doi.org/10.1029/2019GL083542

Ham, S.-H., Kato, S., Rose, F. G., Winker, D., L'Ecuyer, T., Mace, G., et al. (2017). Cloud occurrences and cloud radiative effects (CREs) from CERES-CALIPSO-CloudSat-MODIS (CCCM) and CloudSat radar-lidar (RL) products. *Journal of Geophysical Research: Atmospheres*, *122*(16), 8852–8884. https://doi.org/10.1002/2017JD026725

Hartmann, D. L., Hendon, H. H., & Houze, R. A. (1984). Some implications of the mesoscale circulations in tropical cloud clusters for large-scale dynamics and climate. *Journal of the Atmospheric Sciences*, *41*(1), 113–121. https://doi.org/10.1175/1520-0469(1984)041<0113:SIOTMC>2.0.CO;2

Hartmann, D. L., Holton, J. R., & Fu, Q. (2001). The heat balance of the tropical tropopause, cirrus, and stratospheric dehydration. *Geophysical Research Letters*, *28*(10), 1969–1972. https://doi.org/10.1029/2000gl012833

Haynes, J. M., Haar, V. T. H., L'Ecuyer, T., & Henderson, D. (2013). Radiative heating characteristics of Earth's cloudy atmosphere from vertically resolved active sensors. *Geophysical Research Letters*, *40*(3), 624–630. https://doi.org/10.1002/grl.50145

Henderson, D. S., L'Ecuyer, T., Stephens, G., Partain, P., & Sekiguchi, M. (2013). A multisensor perspective on the radiative impacts of clouds and aerosols. *Journal of Applied Meteorology and Climatology*, *52*(4), 853–871. https://doi.org/10.1175/JAMC-D-12-025.1

Hersbach, H., Bell, B., Berrisford, P., Hirahara, S., Horányi, A., Muñoz-Sabater, J., et al. (2020). The ERA5 global reanalysis. *Quarterly Journal of the Royal Meteorological Society*, *146*(730), 1999–2049. https://doi.org/10.1002/qj.3803

Jeevanjee, N., & Fueglistaler, S. (2020). Simple spectral models for atmospheric radiative cooling. *Journal of the Atmospheric Sciences*, *77*(2), 479–497. https://doi.org/10.1175/JAS-D-18-0347.1

Kato, S., Ham, S.-H., Miller, W. F., Sun-Mack, S., Rose, F. G., Chen, Y., & Mlynczak, P. E. (2021). *Variable descriptions of the A-train integrated CALIPSO, CloudSat, CERES, and MODIS merged product (CCCM or C3M)*. NASA. Retrieved from https://ceres.larc.nasa.gov/documents/collect_guide/pdf/c3m_variables.RelD1.20211117.pdf

L'Ecuyer, T. S., Wood, N. B., Haladay, T., Stephens, G. L., & Stackhouse, P. W. (2008). Impact of clouds on atmospheric heating based on the R04 CloudSat fluxes and heating rates data set. *Journal of Geophysical Research*, *113*, D00A15. https://doi.org/10.1029/2008JD009951

Li, Y., & Thompson, D. W. J. (2016). Observed signatures of the barotropic and baroclinic annular modes in cloud vertical structure and cloud radiative effects. *Journal of Climate*, *29*(13), 4723–4740. https://doi.org/10.1175/JCLI-D-15-0692.1

Li, Y., Thompson, D. W. J., Huang, Y., & Zhang, M. (2014). Observed linkages between the northern annular mode/North Atlantic oscillation, cloud incidence, and cloud radiative forcing. *Geophysical Research Letters*, *41*(5), 1681–1688. https://doi.org/10.1002/2013GL059113

Li, Y., Thompson, D. W. J., Stephens, G. L., & Bony, S. (2014). A global survey of the instantaneous linkages between cloud vertical structure and large-scale climate. *Journal of Geophysical Research: Atmospheres*, *119*(7), 3770–3792. https://doi.org/10.1002/2013JD020669

Lipat, B. R., Voigt, A., Tselioudis, G., & Polvani, L. M. (2018). Model uncertainty in cloud–circulation coupling, and cloud-radiative response to increasing CO2, linked to biases in climatological circulation. *Journal of Climate*, *31*(24), 10013–10020. https://doi.org/10.1175/JCLI-D-17-0665.1

Mace, G. G., & Zhang, Q. (2014). The CloudSat radar-lidar geometrical profile product (RL-GeoProf): Updates, improvements, and selected results. *Journal of Geophysical Research: Atmospheres*, *119*(15), 9441–9462. https://doi.org/10.1002/2013JD021374

McCoy, D. T., Hartmann, D. L., & Grosvenor, D. P. (2014). Observed Southern Ocean cloud properties and shortwave reflection Part I: Calculation of SW flux from observed cloud. *Journal of Climate*, *27*(23), 8836–8857. https://doi.org/10.1175/JCLI-D-14-00287.1

Oreopoulos, L., Cho, N., & Lee, D. (2017). New insights about cloud vertical structure from CloudSat and CALIPSO observations. *Journal of Geophysical Research: Atmospheres*, *122*(17), 9280–9300. https://doi.org/10.1002/2017JD026629

Papavasileiou, G., Voigt, A., & Knippertz, P. (2020). The role of observed cloud-radiative anomalies for the dynamics of the North Atlantic oscillation on synoptic time-scales. *Quarterly Journal of the Royal Meteorological Society*, *146*(729), 1822–1841. https://doi.org/10.1002/qj.3768

Schäfer, S., & Voigt, A. (2018). Radiation weakens idealized midlatitude cyclones. *Geophysical Research Letters*, *45*(6), 2833–2841. https://doi.org/10.1002/2017GL076726

Slingo, A. (1989). A GCM parameterization for the shortwave radiative properties of water clouds. *Journal of the Atmospheric Sciences*, *46*(10), 1419–1427. https://doi.org/10.1175/1520-0469(1989)046<1419:agpfts>2.0.co;2

Stephens, G. L., Vane, D. G., Boain, R. J., Mace, G. G., Sassen, K., Wang, Z., et al. (2002). The CloudSat mission and the A-train: A new dimension of space-based observations of clouds and precipitation. *Bulletin of the American Meteorological Society*, *83*(12), 1771–1790+1742. https://doi.org/10.1175/BAMS-83-12-1771

Thompson, D. W. J., & Wallace, J. M. (2000). Annular modes in the extratropical circulation. Part I: Month-to-month variability. *Journal of Climate*, *13*(5), 1000–1016. https://doi.org/10.1175/1520-0442(2000)013<1000:AMITEC>2.0.CO;2

Thompson, D. W. J., & Woodworth, J. D. (2014). Barotropic and baroclinic annular variability in the southern hemisphere. *Journal of the Atmospheric Sciences*, *71*(4), 1480–1493. https://doi.org/10.1175/JAS-D-13-0185.1

Voigt, A., Albern, N., Ceppi, P., Grise, K., Li, Y., & Medeiros, B. (2021). Clouds, radiation, and atmospheric circulation in the present-day climate and under climate change. *Wiley Interdisciplinary Reviews: Climate Change*, *12*(2), 1–22. https://doi.org/10.1002/wcc.694

Voigt, A., & Shaw, T. A. (2015). Circulation response to warming shaped by radiative changes of clouds and water vapour. *Nature Geoscience*, *8*(2), 102–106. https://doi.org/10.1038/ngeo2345

Voigt, A., & Shaw, T. A. (2016). Impact of regional atmospheric cloud radiative changes on shifts of the extratropical jet stream in response to global warming. *Journal of Climate*, *29*(23), 8399–8421. https://doi.org/10.1175/JCLI-D-16-0140.1

Wall, C. J., Hartmann, D. L., & Ma, P.-L. (2017). Instantaneous linkages between clouds and large-scale meteorology over the Southern Ocean in observations and a climate model. *Journal of Climate*, *30*(23), 9455–9474. https://doi.org/10.1175/JCLI-D-17-0156.1

Watt-Meyer, O., & Frierson, D. M. W. (2017). Local and remote impacts of atmospheric cloud radiative effects onto the eddy-driven jet. *Geophysical Research Letters*, *44*(19), 10036–10044. https://doi.org/10.1002/2017GL074901